

Adjacent MnO_x clusters enhance the hydroformylation activity of rhodium single-atom catalysts

Ying Zheng ^{a,b,c}, Qi Yang ^a, Sikai Wang ^{b,c}, Shinya Furukawa ^d, Maoshuai Li ^{a,*}, Ning Yan ^{b,c,**}, Xinbin Ma ^{a,*}

^a Key Laboratory for Green Chemical Technology of Ministry of Education, School of Chemical Engineering and Technology, Haihe Laboratory of Sustainable Chemical Transformations, Tianjin University, Tianjin 300350, China

^b Joint School of National University of Singapore and Tianjin University, International Campus of Tianjin University, Binhai New City, Fuzhou 350207, China

^c Department of Chemical and Biomolecular Engineering, National University of Singapore, 117585, Singapore

^d Institute for Catalysis, Hokkaido University, N-21, W-10, Sapporo 001-0021, Japan



ARTICLE INFO

Keywords:

Propylene hydroformylation
Butyraldehyde
Single atom
Rh-MnO_x pair
Mechanism

ABSTRACT

Hydroformylation reactions promoted by Rh single-atom catalysts typically exhibit a negative reaction order for CO and a positive reaction order for H₂ and alkenes. To enhance the catalytic activity, efforts have been concentrated on reducing the CO adsorption strength and/or enhancing the hydrogenation capacity at Rh sites. This report introduces an optimized Rh single-atom catalyst, utilizing positively charged Mn species to weaken the CO adsorption strength. Our strategy involves placing MnO_x clusters in the proximity to the Rh single atom. This arrangement allows the reduction of Rh³⁺ to produce electronically deficient Rh^{δ+} species (1 < δ < 2), rather than the usual formation of the lower valence state Rh⁺ species. The weakened CO adsorption strength on the more positively charged Rh^{δ+} results in reduced CO coverage on the Rh active site, and enhanced adsorption of propylene. Our mechanistic study reveals that H₂ and CO adsorption on Rh catalyzes the reduction of adjacent Mn(IV) species, inducing the formation of a Rh-MnO_x paired active site. The neighboring MnO_x clusters hinder the extensive reduction of Rh³⁺ to Rh⁺. This study presents MnO_x as an inorganic ligand in Rh-MnO_x pair site modifies the electronic properties of Rh sites to modulate the hydroformylation activity of Rh single-atom catalysts.

1. Introduction

The hydroformylation of olefins is one of the most significant industrial processes because the related product, aldehydes, are widely used as intermediates for synthesis of alcohols, esters, carboxylic acids and other fine chemicals [1,2]. Rh-based homogeneous catalysts are widely applied due to their outstanding activity and selectivity [3–5]. Compared with homogeneous catalysts, heterogeneous catalysts have lower activity and selectivity, but can be more easily recovered from the reaction mixture [1,2]. As the bridge between homogeneous and traditional heterogeneous catalysts, single atom catalysts (SAC) are expected to serve as catalysts for hydroformylation reactions with both high activity and selectivity [6,7].

Based on the mechanism of homogeneously catalysed

hydroformylation proposed by Heck and Breslow [8,9], the catalytic cycle involves: (I) activation of the catalyst by dissociation of one ligand, (II) the oxidative addition of olefin, (III) olefine insertion into the Rh-H bond, (IV) CO coordination, (V) CO insertion, (VI) oxidative addition of H₂, (VII) reductive elimination of the resulting aldehyde with four transition states (TS) [4,10]. All these steps are possible to be the rate-limiting step (RLS), depending on the nature of the catalyst, reaction condition, and olefin etc. [4,10,11]. In homogeneous systems, most experimental and theoretical studies acknowledged that either olefine insertion into the Rh-H bond or reductive elimination of the resulting aldehyde, to be the RLS [12–14]. In many heterogeneous systems, CO insertion was the most energetically demanding step, for example, on Rh/MgO, Rh/CeO₂, Rh/ReO_x-Al₂O₃, Rh/WO_x-Al₂O₃, Rh(111), and RhCo(111) surfaces [11,15–18]. The reaction order of CO in the olefin

* Corresponding authors.

** Corresponding author at: Joint School of National University of Singapore and Tianjin University, International Campus of Tianjin University, Binhai New City 350207, China.

E-mail addresses: maoshuaili@tju.edu.cn (M. Li), ning.yan@nus.edu.sg (N. Yan), xbma@tju.edu.cn (X. Ma).

hydroformylation reaction is negative [16,19–22] due to the strong adsorption of CO on Rh. When CO insertion is the RLS, the key factor that improves reaction activity is to weaken CO adsorption strength to benefit its desorption and attack to hydrogenated olefine on SAC [10,11, 15]. Efforts to regulate the CO adsorption strength on Rh active centers have been reported, often involving the integration of a secondary inactive component. For example, the introduction of RhP₂ [23], Rh-ReO_x [16,24], and Rh-WO_x [17] has been shown to draw electrons away from the Rh center. The key role of oxygen vacancy on support surface has been founded for reducible supports of CeO₂[18] and SnO₂ [25] supported Rh SAC systems, which can modulate the direct coordination environment in single atom sites, via the exploitation of the oxide support's surface chemistry. Single-atom Rh/CeO₂ was also active for the hydroformylation of styrene coupled with water-gas shift reaction that benefitted the linear product formation [26]. Alternatively, the formation of intermetallic compounds such as RhZn [27] and RhCo [15] has also been employed. This approach leverages the separation (dilution) effects of the secondary inactive component to reduce the overly robust adsorption of CO.

Well-recognized for its varied and tunable valence states, in addition to practical advantages such as abundance and affordability, Mn has been deployed as a promoter to improve the activity of noble metal catalysts. Among currently reported systems, Rh catalysts promoted by MnO_x are among the most effective for converting syngas into ethanol and other C₂₊ oxygenates such as acetaldehyde and acetic acid [28–30]. The MnO_x promoter functions as an electron-withdrawing ligand, partially oxidizing Rh atoms at the Rh-MnO_x interface, which enhances the CO insertion in the desired reaction [28,30,31]. MnO_x has also been demonstrated to control the electronic property of Pd in CO₂ hydrogenation reactions [32]. However, to the best of our knowledge, no systematic investigation has been conducted on the role of single-atom Rh-MnO_x in hydroformylation reactions. As such, we seek to employ the electronic interaction between MnO_x and Rh to diminish the CO adsorption strength on Rh, thereby enhancing the hydroformylation capability. To achieve highly dispersed and stable MnO_x species, CeO₂ as the support has been selected due to its strong interaction with Mn [33–35].

In this study, we describe the synthesis, characterization, and comparative catalytic performance of the Rh-MnO_x/CeO₂ catalyst versus the Rh/CeO₂ catalyst prepared by the static electronic adsorption (SEA) method. Encouragingly, the Rh-MnO_x/CeO₂ catalyst indeed exhibited superior hydroformylation activity compared to the Rh/CeO₂ catalyst. We further studied the catalyst structural transformation and explored the mechanism underlying the enhanced activity. Specifically, X-ray photoelectron spectroscopy (XPS) and CO probe molecule Fourier Transform Infrared Spectroscopy during Temperature-Programmed Desorption (CO-FTIR-TPD) were used to determine the electronic structure and CO adsorption property, while *pseudo in-situ* XPS and *in-situ* FTIR spectroscopy were employed to identify the active species and its transformation under reaction condition.

2. Experimental and computational section

2.1. Catalyst preparation

y %MnO_x/CeO₂ samples were prepared by incipient wetness impregnation method. In detail, the CeO₂ cube (synthesis method is described in SI) was immersed in appropriate amounts of aqueous solution of Mn (NO₃)₂ • 4 H₂O for 48 h then dried overnight at 80 °C and followed by calcination at 400 °C for 4 h. The obtained samples were labelled as y %MnO_x/CeO₂, where y represents the mass loading of Mn (y = 0.5, 1, 2.5 and 5).

Rh/y %MnO_x-CeO₂ samples were prepared by SEA method. Typically, y %MnO_x/CeO₂ support was impregnated by appropriate amounts of aqueous solution of [(NH₂CH₂CH₂NH₂)₃RhCl₃ under stirring, the solution pH was adjusted to 8 as determined by experiments in SI. Then,

the samples were obtained by washing with deionized water, centrifugal filtration, and drying at 80 °C for 12 h. Subsequently, the samples were calcined at 800 °C for 10 h. The resultant catalysts were labelled as Rh-y %MnO_x/CeO₂.

2.2. Catalytic activity test

The hydroformylation of propylene was performed in a 100 mL stainless-steel autoclave. After the addition of catalysts and 10 mL of n-heptane as solvent, the autoclave was pressurized with propylene (0.2 MPa), 1:1 molar ratio of CO and H₂ mixture (3 MPa). The reaction was performed at 100 °C with stirring at 300 rpm. After the completion of the reaction, the gas-phase components were collected and analyzed by gas chromatography (GC) using a Flame Ionization Detector (FID) detector. The liquid-phase components in the autoclave were collected by filtrating the reaction solution with a 0.45 μm polyethersulfone syringe filter and analysed by GC-FID using n-hexane as an internal standard. The filtrate was subjected to GC on a GC-2014-Shimadzu with a WondaCap FFAP capillary column and an FID. The recyclability of the catalyst was tested by centrifugal separation, and it was reused for the next run without washing. The kinetic study was conducted under the conversions <25 % by changing the catalyst mass. The reaction order of each reactant (CO, H₂, C₃H₆) was studied by changing the pressure of one gas with the same total pressure by introducing Ar as balance gas.

2.3. Characterization

High-Angle Annular Dark-Field Scanning Transmission Electron Microscopy (HAADF-STEM) analysis was carried out by a JEM-ARM200F microscope equipped with a spherical aberration collector at 200 kV. X-ray absorption spectroscopy (XAS) including extended X-ray absorption fine structure (EXAFS) and X-ray fine near-edge structure (XANES) at Rh K-edge were taken at the BL14B2 beamline at SPring-8 (Japan Synchrotron Radiation Research Institute, Hyogo, Japan) in fluorescence mode. IFEFFIT and Demeter packages were used as included in Athena and Artemis for the reduction of data (k range: 3–12). The X-ray edge energy was estimated using the first maximum of the first derivative of the absorption intensity. X-ray photoelectron spectroscopy (XPS) was conducted on a K-Alpha⁺ spectrometer produced by Thermo Fisher Scientific. The X-ray source is Al K_α (1486.6 eV) and the X-rays were monochromated. The calibration of the binding energy of Rh and Ce was based on that of C 1 s (284.8 eV) as the correction value. The sample was treated with CO, H₂, C₃H₆, CO+H₂, or CO+H₂+C₃H₆ (1 bar) at 100 °C for 0.5 h in the fix bed reactor, after which it was transferred into the vacuum transfer stage in glove box for XPS measurement without exposure to air. *In-situ* FTIR spectroscopy was conducted by adsorption of CO and H₂ (molar ratio of CO: H₂ = 1:1) on catalyst until saturation, then purging off physically adsorbed species with the chemically adsorbed CO* and H* on Rh remained as active species. The reactivity of the adsorbed CO* and H* was investigated by introducing C₃H₆ to the IR cell. The reaction of the pre-adsorbed CO* and H* with C₃H₆ was carried out at 100 °C and a pressure of 1 atm. The *in-situ* FTIR spectra were collected under atmospheric pressure and gas phase, different from the catalytic evaluation condition.

3. Discussion

3.1. Establishment of Rh/MnO_x-CeO₂ catalysts with different MnO_x dispersion

MnO_x/CeO₂ was initially prepared via the impregnation method, followed by calcination at 400 °C. Subsequently, Rh was loaded using the SEA method and calcined at 800 °C (Figure S1-S3). At specific pH range, the ion (H⁺ or OH⁻) that lies on the surface of MnO_x and CeO₂ can be different because of the different PZC values of the metal oxides. Rh and MnO_x islands are expected to be located near each other since the

pH of the $[(\text{H}_2\text{NCH}_2\text{CH}_2\text{NH}_2)_3\text{Rh}]^{3+}$ impregnation solution was adjusted to 8. This value is higher than the PZC of MnO_x but lower than that of CeO₂. At a pH of 8, MnO_x surface carries a negative charge while the surface of CeO₂ is positively charged, resulting in the positively charged $[(\text{H}_2\text{NCH}_2\text{CH}_2\text{NH}_2)_3\text{Rh}]^{3+}$ being attracted to MnO_x and repelled by CeO₂ (Scheme S1)[36,37]. Following this protocol, we established a series of Rh/MnO_x-CeO₂ catalysts featuring a 0.06 % Rh loading amount and Mn loading amounts ranging from 0 % to 5 %. We also prepared MnO_x/CeO₂ with Mn loading amounts varying between 0.5 % and 5 % as control samples. Inductively coupled Plasma-Optical Emission Spectrometer (ICP-OES)-determined actual loading amounts of Rh and Mn are listed in Table S1. After loading Mn and Rh, the Brunauer-Emmett-Teller (BET) surface area and pore size distribution of CeO₂ remained consistent (Figure S4 and Table S2).

High-resolution transmission electron microscopy (HRTEM) images displayed in Fig. 1(a) and (b) confirm the successful preparation of CeO₂ nanocubes, with rounded edges observed after calcination at 800°C. EDS mapping reveals a high dispersion of Mn species on 1 %MnO_x/CeO₂ and Rh/1 %MnO_x-CeO₂ catalysts. Analysis of the X-Ray Diffraction (XRD) pattern (Fig. 1(c)) demonstrate an expansion of the CeO₂ crystal cell, as evidenced by a peak shift of 0.11°. Moreover, the Raman spectra (Fig. 1 (d)) indicated an increased amount of oxygen vacancies, as reflected by the higher ratio value of I_D/I_{F2g} . In detail, the signal at 465 cm⁻¹ corresponds to the F_{2g} symmetry mode of the CeO₂ phase, while the weak

band at approximately 600 cm⁻¹ is associated with oxygen vacancies (D band) [38,39]. The intensity ratio of these two peaks (I_D/I_{F2g}) provides information about the concentration of the oxygen vacancies [40]. The enhanced concentration of oxygen vacancies was attributed to the strong interaction between Mn single atoms or MnO_x clusters and CeO₂, resulting in the incorporation of Mn cations into the CeO₂ lattice and the formation of oxygen vacancies to maintain the electronic properties of CeO₂[41–45]. The XRD analysis of the 5 % Mn-doped catalyst reveals peaks attributed to bulky MnO₂. Similarly, the Raman spectra detected a vibration signal near 641 cm⁻¹, attributable to MnO₂[46], in the 2.5 % and 5 % Mn-doped samples. Thus, when the Mn doping amount is below 1 %, the Mn species exhibit high dispersion on the surface of CeO₂, leading to its incorporation into the CeO₂ lattice. A MnO₂ bulk phase is formed for the Mn doping amount >1 %.

HAADF-STEM, EXAFS, and CO-FTIR results indicate atomically dispersed Rh located near MnO_x (Fig. 2). Rh (the light dot) is positioned adjacent to the MnO_x island rather than on CeO₂ as evident in HAADF-STEM images (Fig. 2(a)). It should be mentioned that the atomic number of Ce (58) is higher than that of Rh (45); the bright dots observed in the HAADF-STEM image are ascribed to the Rh single atoms only when viewed through the direction of the off-axis [47–49]. XANES profiles (Fig. 2(b)) suggest Rh is proximate to Rh³⁺ state before reaction for both Rh/CeO₂ and Rh/MnO_x-CeO₂ samples, because the edge energy and the white line intensity for all Rh samples closely resembled that of the

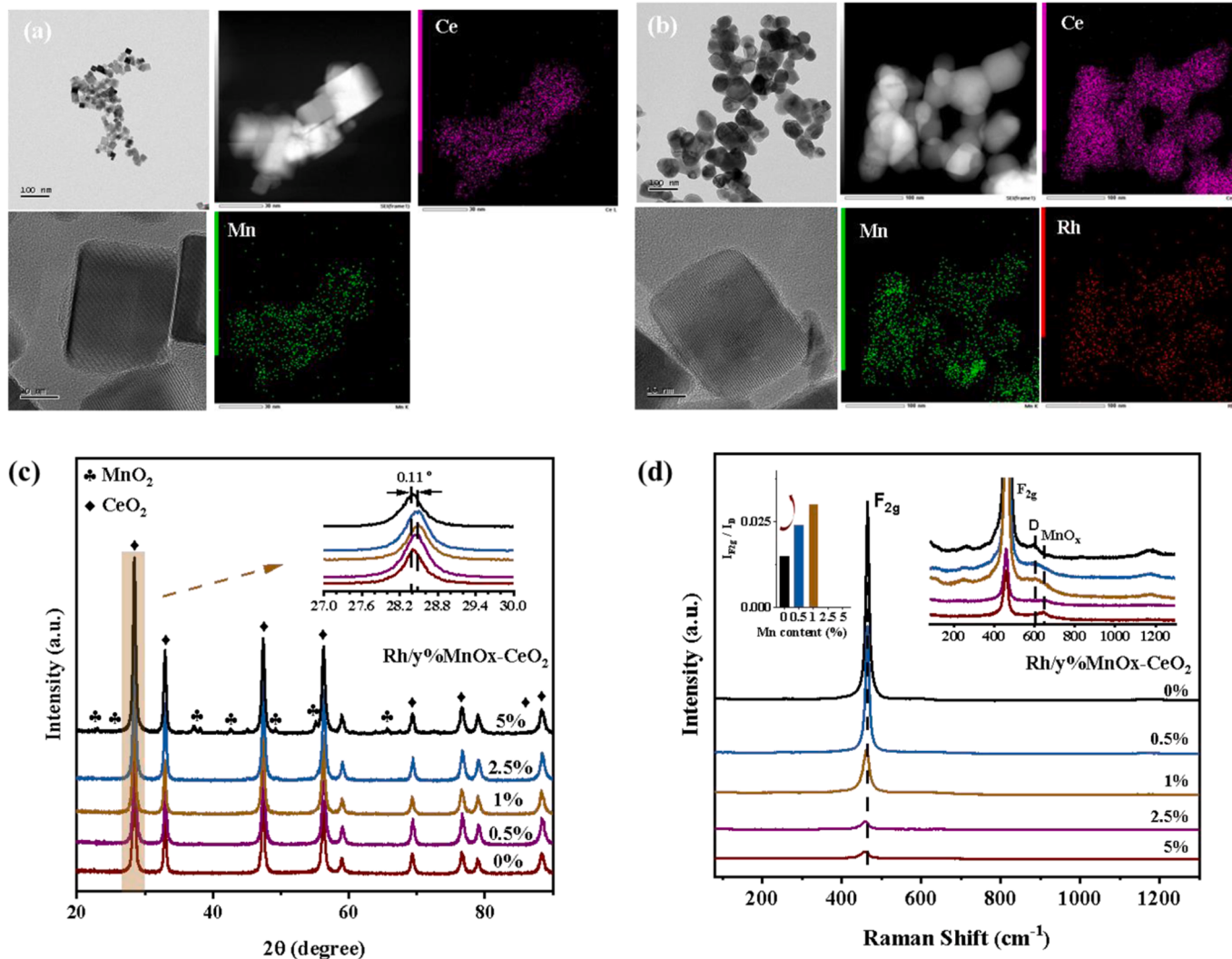


Fig. 1. HRTEM and mapping images of (a) 1 %MnO_x/CeO₂ and (b) Rh/1 %MnO_x-CeO₂ samples. (c) XRD patterns and (d) Raman spectra of Rh/y %MnO_x-CeO₂, where y % represent the mass percentage of Mn on CeO₂.

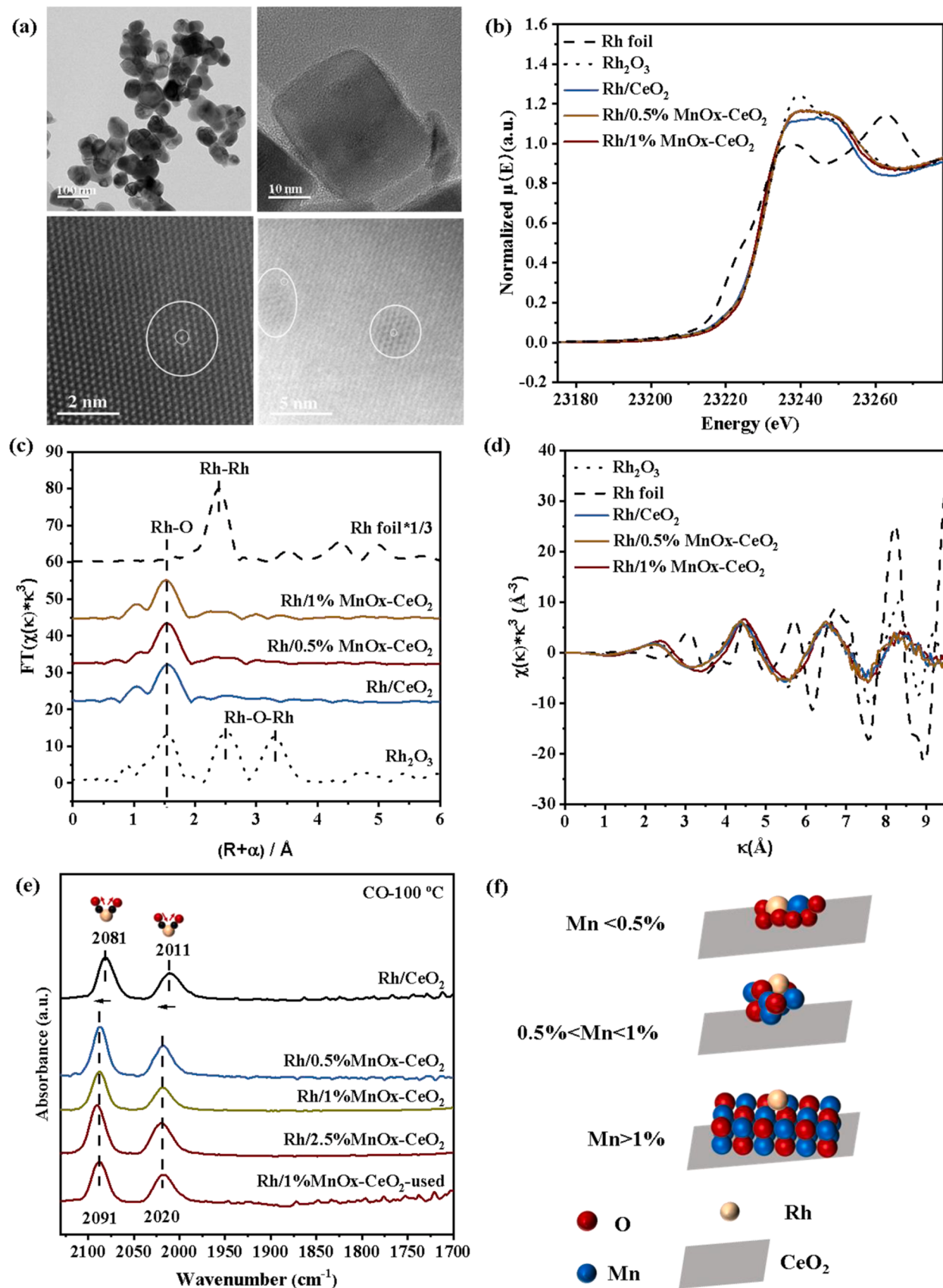


Fig. 2. (a) TEM and HAADF-STEM images of Rh/1%MnOx-CeO₂, (b) Rh K-edge XANES profiles, (c) Rh K-edge EXAFS spectra shown in R space, (d) Rh K-edge EXAFS shown in k^3 -weighted k -space for Rh foil, Rh₂O₃, and Rh/y%MnOx-CeO₂, (e) CO-FTIR spectra, and (f) proposed structure scheme of Rh/y%MnOx-CeO₂ with different Mn amounts (y %).

Rh_2O_3 reference. A blue shift (2081 and 2011 cm^{-1} to 2091 and 2020 cm^{-1}) of bands attributed to $\text{Rh}(\text{CO})_2$ species in the CO probe molecule-FTIR spectra (Fig. 2(e)) reveals the electronic interaction between Rh and adjacent MnO_x . The Rh K-edge EXAFS profiles in Fig. 2(c) and fitting curves in Figure S5 unveil a first shell at approximately 1.5 Å corresponding to Rh-O, with no presence of Rh-Rh shell at roughly 2.5 Å, suggesting atomically dispersed Rh species for all the Rh/CeO_2 and $\text{Rh}/y\% \text{MnO}_x\text{-CeO}_2$ catalysts. The Rh K-edge EXAFS spectra in Fig. 2(d) demonstrate that $\text{Rh}/y\% \text{MnO}_x\text{-CeO}_2$ and Rh/CeO_2 profiles more closely resemble Rh_2O_3 than Rh foil. The CO probe molecule FTIR spectroscopy analysis in Fig. 2(e) displays typical symmetric and asymmetric stretching vibration modes (around 2091 and 2020 cm^{-1}) of the positively charged $\text{Rh}(\text{CO})_2$ species for all the $\text{Rh}/y\% \text{MnO}_x\text{-CeO}_2$ catalysts. The absence of a band ($1700 - 1800 \text{ cm}^{-1}$) attributed to CO bridge adsorption on Rh cluster/nanoparticle, further confirms the atomic dispersion of Rh. From these characterizations, we depict a catalyst structure with varying dispersion of Mn species in Fig. 2(f). When the Mn loading amount is less than 0.5 %, Rh and Mn are atomically dispersed; at a Mn amount of 1 %, Rh is located on MnO_x cluster; further increasing the Mn amount to more than 1 % leads to a MnO_2 nanoparticle supported single-atom Rh structure.

3.2. Catalytic reactivity for propylene hydroformylation

In a syngas atmosphere, propylene can be hydrogenated to propane or undergo hydroformylation to butyraldehyde. During hydroformylation, CO is inserted into the terminal and internal positions of the C=C bond in propylene, yielding linear and branched butyraldehyde, respectively. The catalytic performance of Rh/CeO_2 and $\text{Rh}/y\% \text{MnO}_x\text{-CeO}_2$ was evaluated in propylene hydroformylation under 3 MPa syngas and 100 °C. Before measurements, it has been confirmed that no thermodynamic equilibrium or mass transfer limitations exist in the system (Figure S6). As shown in Fig. 3(a), only butyraldehyde was formed as the product, demonstrating 100 % chemo-selectivity. The Turnover Frequency (TOF) exhibits a volcano-shaped curve with increasing Mn amounts for hydroformylation, achieving the highest value (~ 7200 h⁻¹) at Mn amount = 1 %. The ratio of linear to branched butyraldehyde (l/b), an indicator of regio-selectivity, remains constant at ~0.67 as the Mn amount increases, suggesting that Mn addition does not impact the regio-selectivity for Rh. Although the catalyst system has no steric hindrance effect, the l/b ratio is not 1 but 0.67, indicating that the catalyst structure and reaction condition in this work prefer the formation of iso-butanal. Fig. 3(b) shows that $\text{Rh}/1\% \text{MnO}_x\text{-CeO}_2$ exhibits the lowest apparent activation barrier (E_a) for butyraldehyde formation, possibly because the Mn doping aids the formation of more active Rh species for propylene hydroformylation.

The recyclability of $\text{Rh}/1\% \text{MnO}_x\text{-CeO}_2$ was evaluated by conducting successive rounds of reaction (Fig. 3(c)). Remarkably, 90 % of the original activity was retained after five cycles. According to the CO-FTIR result (Fig. 2(e)), the Rh species post-reaction remained atomically dispersed. Negligible activity (<5 %) was detected in the supernatant obtained by filtering the catalysts from the reaction solution, reinforcing that the catalytic activity primarily stems from the Rh supported on CeO_2 , not from the leached Rh species.

The power law equation for propylene hydroformylation can be expressed as

$$r = kP_{\text{CO}}^\alpha P_{\text{H}_2}^\beta P_{\text{C}_3\text{H}_6}^\gamma$$

in which k and P_{CO} , P_{H_2} , $P_{\text{C}_3\text{H}_6}$ stand for the reaction rate constant and the partial pressure of CO, H₂, and C₃H₆, respectively; while α , β and γ are the reaction order for CO, H₂ and C₃H₆, respectively. As illustrated in Fig. 3(d-f), the values calculated for CO (α), H₂ (β), and C₃H₆ (γ) at 100 °C for $\text{Rh}/1\% \text{MnO}_x\text{-CeO}_2$ are -0.44, 0.36, and 0.52, respectively. Compared with Rh/CeO_2 ($\alpha = -1.2$), the reactor order of CO has moved towards a less negative value. This implies that CO is more weakly

adsorbed on Rh, a finding further confirmed by the CO-FTIR-TPD and CO-TPD results showing a reduction in the strength of CO adsorption over $\text{Rh}/1\% \text{MnO}_x\text{-CeO}_2$. The weakened CO adsorption is beneficial for C₃H₆ adsorption, as evidenced by the reduced C₃H₆ order (γ) value from 0.94 on Rh/CeO_2 to 0.52 on the $\text{Rh}/1\% \text{MnO}_x\text{-CeO}_2$ catalyst.

The H₂ order (β) for $\text{Rh}/1\% \text{MnO}_x\text{-CeO}_2$ ($\beta = 0.36$) is similar to that of Rh/CeO_2 ($\beta = 0.42$), signifying that 1 % MnO_x doping doesn't impede H₂ activation. In contrast, the H₂ reaction order for the catalyst doped with 2.5 % Mn significantly escalates to 0.94, suggesting a hampered H₂ activation ability. H₂-TPR and H₂-TPD results reveal a high reduction temperature (starting from 150 °C) for RhO_x on the 2.5 % Mn-doped catalyst, suggesting increased barrier for Rh³⁺ reduction due to the diminished H₂ adsorption strength.

For these experiments, the $\text{Rh}/y\% \text{MnO}_x\text{-CeO}_2$ ($y < 1\%$) catalysts bearing Rh-MnO_x clusters exhibit enhanced CO reaction order and reduced C₃H₆ reaction order. This pattern, coupled with a lower activation energy, suggests that the Rh-MnO_x cluster active species can mitigate the vigorous adsorption of CO on Rh and facilitates the adsorption of C₃H₆, thereby enhancing the overall activity.

3.3. The modification of CO adsorption property on Rh by adjacent MnO_x species

We conducted a series of TPR and TPD experiments to explore the metal-support interactions and CO adsorption property in different catalysts. The H₂-TPR profile of pure CeO_2 (Fig. 4(a)) features two peaks, attributable to the reduction of surface CeO_2 (around 380 °C) and bulk CeO_2 (approximately 720 °C). For Rh/CeO_2 and $\text{Rh}/\text{MnO}_2\text{-CeO}_2$, the hydrogen consumption for the peak at 50–200 °C was estimated to be 2–4.5 mmol/g, much higher than the theoretical amount (8.7 $\mu\text{mol/g}$) needed for Rh³⁺ reduction (Figure S4). The remaining hydrogen was plausibly used for surface reduction of MnO_x and CeO₂. The introduction of Rh stimulates the co-reduction of RhO_x and surface CeO₂ (around 90 °C). Likewise, $\text{Rh}/y\% \text{MnO}_x\text{-CeO}_2$ allows for the co-reduction of MnO_x, RhO_x , and surface CeO₂. Due to the atomic dispersion of Rh, there is only Rh-O-Ce structure around Rh for Rh/CeO_2 catalysts, which is reduced at 88 °C as indicated by the first signal in Fig. 4(a). Likewise, only Rh-O-Mn structure around Rh center is existed for Rh/MnO_2 catalyst, which showed a much higher reduction temperature (246 °C) (Figure S7). Thus, as the Mn content increased to 2.5 %, more Rh-O-Mn structure is formed, shifting the peak temperature from 88 °C to 230 °C (Fig. 4(a)). This observation aligns with XPS results demonstrating a gradual decrease in Rh's electronic density with increasing MnO_x loading amount for $\text{Rh}/y\% \text{MnO}_x\text{-CeO}_2$ (Fig. 4(b)), which may stem from the strong interaction between Rh and MnO_x-CeO₂. In line with this, the band doublet attributed to the symmetric and asymmetric stretching of $\text{Rh}(\text{CO})_2$ species on Mn-doped catalysts (~2086 and ~2015 cm^{-1}) showed a blue shift compared with that on Rh/CeO_2 (2079 and 2008 cm^{-1}), hinting at a lower electronic density of single-atom Rh for $\text{Rh}/\text{MnO}_x\text{-CeO}_2$ (Fig. 4(c,d,e,f)). Moreover, the generated Rh^{δ+} species exhibit diminished CO adsorption strength due to the reduction of available electrons for CO coordination (Fig. 4(c,d,e,f)).

The CO-FTIR-TPD spectra (Fig. 4(c)) reveal two signals at 2079 cm^{-1} and 2008 cm^{-1} , linked to the symmetric and asymmetric vibration of single atom Rh(CO)₂ species on Rh/CeO_2 . A 2092 cm^{-1} band is related to single-atom Rh(CO) species, which also has been observed in $\text{Rh}/\gamma\text{-Al}_2\text{O}_3$ [50] and $\text{Rh}/\text{Ce}_x\text{Zr}_{1-x}\text{O}_2$ [51] systems, consequent to the desorption of one CO from Rh(CO)₂ species. Rh(CO)₂ species desorb gradually with temperature increase, persisting at 200 °C for Rh/CeO_2 . For Mn-doped samples at 0.5 %, 1 %, and 2.5 % (Fig. 4(d), (e), and (f)), the CO adsorption strength on single-atom Rh weakens as evidenced by a lower full desorption temperature below 180 °C, compared to over 200 °C on Rh/CeO_2 . As shown in Fig. 4(g) and (h), the CO desorption rate on Rh/CeO_2 is significantly lower than on the Mn-doped samples, further suggesting that Mn doping weakens the CO adsorption strength. Specifically, the CO desorption rate on Rh/CeO_2 is roughly 1/3 of that on

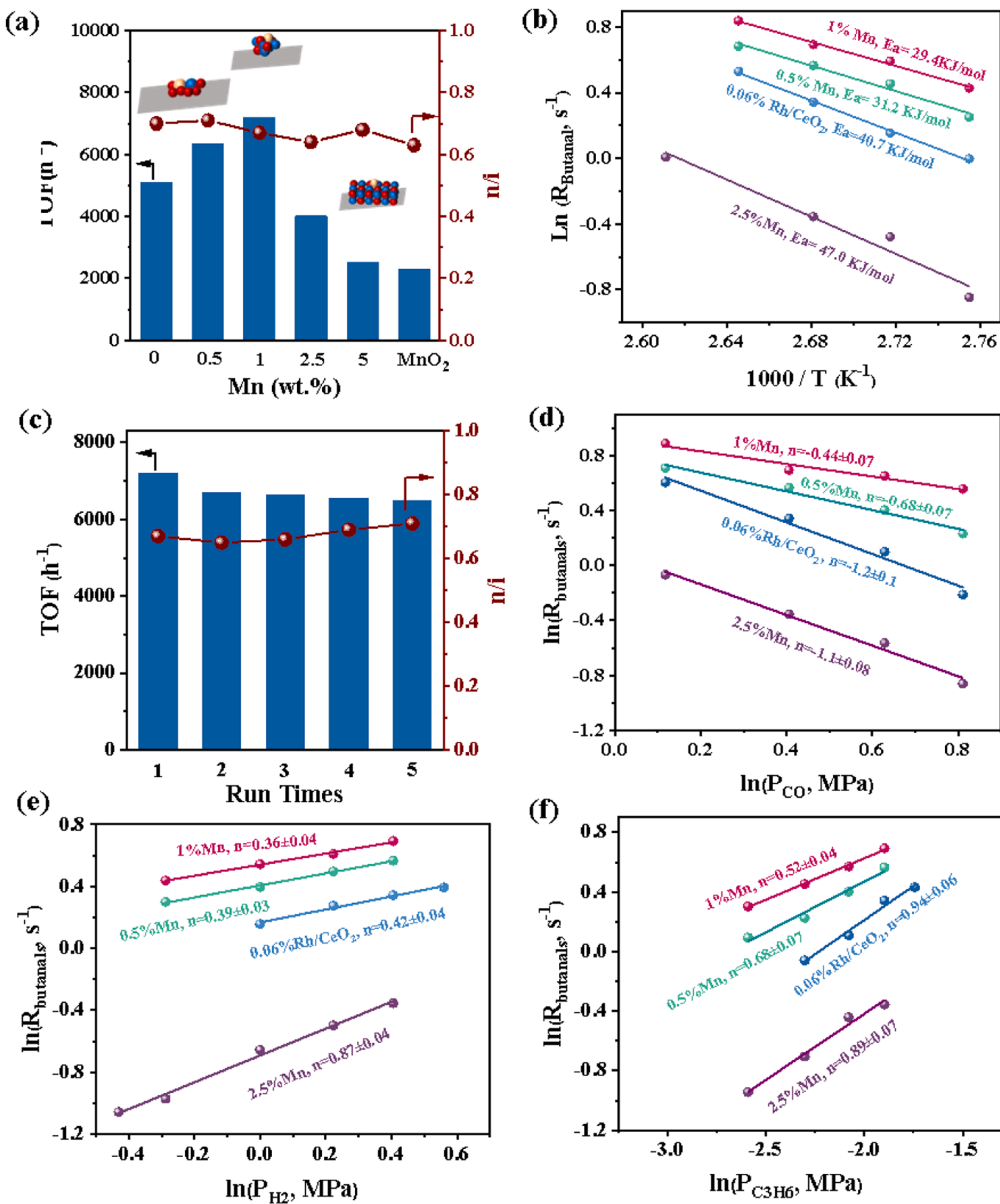


Fig. 3. (a) The effect of Mn amount on TOF and selectivity for 0.06 % Rh/CeO₂-cube. (b) Arrhenius plots of 0.06 % Rh/y %MnO_x-CeO₂ with different amount of Mn. (c) Recycling performance of 0.06 % Rh/1 %MnO_x-CeO₂ for the hydroformylation of propylene. The propylene conversion is between 20 % and 25 %. (d) CO, (e) H₂, and (f) C₃H₆ reaction order of Rh/y %MnO_x-CeO₂ catalysts at 100 °C. Reaction condition: 100 °C, 3 MPa CO/H₂ (1:1), 0.2 MPa propylene, 20 mg catalyst, 0.5 h, 300 rpm. Kinetic experiments were examined under the conversions <25 % by varying the catalyst amount. For determining the reactant orders, make sure P_{Total} = 3.2 MPa, catalyst mass = 0.1 g, (d) P_{C3H6} = 0.2 MPa, P_{H2} = 1.5 MPa, balance gas: He, (e) P_{C3H6} = 0.2 MPa, P_{CO} = 1.5 MPa, balance He, (f) P_{CO} = P_{H2} = 1.5 MPa, balance He.

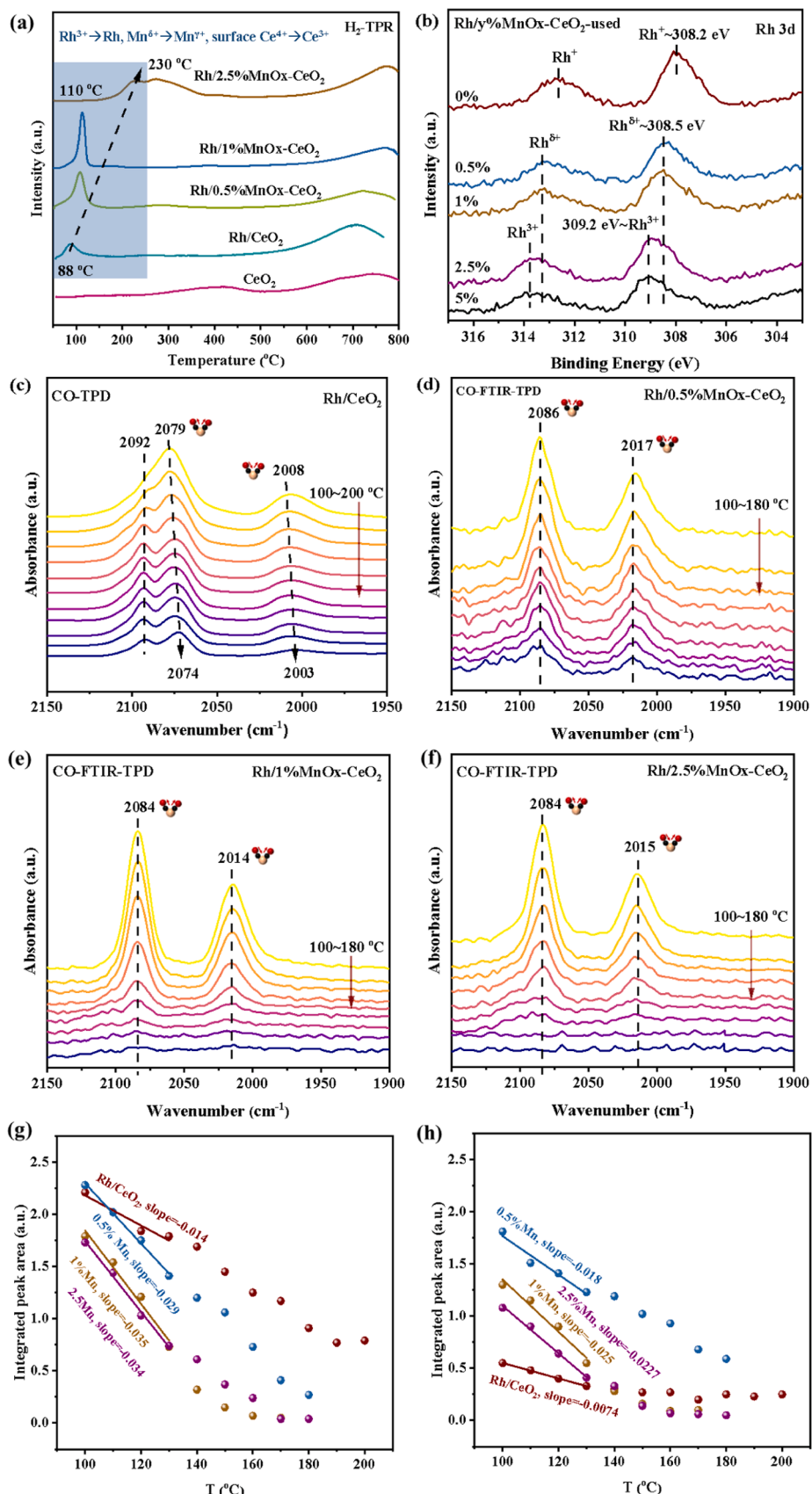


Fig. 4. (a) $\text{H}_2\text{-TPR}$ for $\text{Rh}/y\% \text{MnOx}-\text{CeO}_2$ with different amounts of Mn, (b) Rh 3d XPS spectra for $\text{Rh}/y\% \text{MnOx}-\text{CeO}_2$ with different amount of Mn after reaction. CO-FTIR-TPD spectra for (c) Rh/CeO_2 , (d) $\text{Rh}/0.5\% \text{MnOx}-\text{CeO}_2$, (e) $\text{Rh}/1\% \text{MnOx}-\text{CeO}_2$, and (f) $\text{Rh}/2.5\% \text{MnOx}-\text{CeO}_2$. During CO-FTIR-TPD, CO is adsorbed at 100 $^{\circ}\text{C}$ for 30 min, and the programmed temperature increase rate is 5 $^{\circ}\text{C}/\text{min}$. The evolution of integrated peak area at (g) 2074–2086 cm^{-1} and (h) 2008–2017 cm^{-1} with increasing temperature for Rh/CeO_2 , and $\text{Rh}/x\% \text{MnOx}-\text{CeO}_2$.

the 1 % Mn-doped catalyst. The Rh(CO) species is existed on Rh/CeO₂ sample, but not on Rh/MnOx-CeO₂ sample, due to the weakened CO adsorption strength on Rh after MnOx doping. Hence, relative to Rh⁺ on Rh/CeO₂, Mn doping inhibits the reduction of RhOx to Rh⁺, resulting in Rh^{δ+} species with weaker CO adsorption capacity. Adsorption properties for propylene, H₂, and butanal are discussed in SI (Figure S7-10), and the results show increased adsorption sites for C₃H₆, H₂ and butanal due to the decreased CO adsorption coverage.

3.4. The formation mechanism of Rh-MnOx active species and its role in enhancing hydroformylation activity

We implemented a sequence of spectroscopic analyses under varying reactant conditions to understand the formation mechanism of Rh-MnOx active species. The CO-FTIR results (Fig. 5(a)) exhibit a blue shift (around 10 cm⁻¹) for bands linked to Rh(CO)₂ after incorporating 0.5 % and 1 % Mn to Rh/CeO₂, which aligns with Rh's higher valance state in these catalysts as shown by the XPS analysis (Fig. 4(b)). In the CO-FTIR analysis, OCO*, HCOO*, and CO₂ species were observed on Rh/MnOx-CeO₂ and MnOx-CeO₂ during the co-feeding of CO and H₂ (Fig. 5(c)). The OCO* species gradually strengthen over the HCOO* species, and more CO₂ is generated as the Mn content increases for Rh/MnOx-CeO₂. This suggests that neighbouring MnOx species facilitate the conversion of CO to CO₂, originating from the reduction of Rh and Mn oxide, which matches the formation of CO₂ seen in the CO-TPD results (Figure S11). As shown in the FTIR spectra for MnOx-CeO₂ after treated by reactants (Figure S12), the broad signal within 1950–2150 cm⁻¹ observed on MnOx-CeO₂ samples can be related to CO adsorbed on reduced MnOx cluster surface (denoted as Mn(CO)_x) [29,52,53]. Introducing Rh to MnOx-CeO₂ results in an additional wide band in 1600–1800 cm⁻¹ on 0.5 % and 1 % Mn dopped samples (Fig. 5(b)), which is too low to be caused by a CO bridge bonded to several Rh atoms by carbon atoms alone (normally > 1800 cm⁻¹). Lisitsyn et al. [54] identified comparable frequencies at 1725 cm⁻¹ and 1696 cm⁻¹, which have been hypothesized to be CO on metal/oxide interfacial sites, with C and O being bound to Rh^{δ+} and Mn^{γ+} cations, respectively [55,56]. Based on this, we tend to assign our signal to be related to Rh-C-O-Mn species. The strong IR intensity suggests that a substantial amount of the surface Rh atoms are in close vicinity to Mn cations [57]. The Rh-C-O-Mn entities promote the CO desorption into CO₂, forming Rh(CO) active species. In short, during the process CO adsorbed on Rh reduces the Mn=O bond, aids in CO desorption from Rh(CO)₂, forming the initial Rh(CO) active species. The CO-FTIR results under different reactant treatment (Figure S13) suggest that C₃H₆ adsorption enhances the reduction of MnOx into Mn(CO)x species by CO. This may be due to the steric hindrance effect, whereby the absorption of C₃H₆ causes the migration of CO on Rh to the adjacent Mn=O site, leading to the reduction of MnOx and the formation of Mn(CO)x species.

For the valance state evolution of active species, after introducing CO, the Rh³⁺ (309.2 eV) and Mn⁴⁺ (642.7 eV) species is reduced to Rh^{γ+} (2<γ<3) (308.8 eV) and Mn³⁺ (641.4 eV), which is further reduced to Rh^{δ+} (308.5 eV) and Mn²⁺ (640.4 eV), respectively, after introducing H₂ or/and C₃H₆ under reaction conditions (Fig. 5(d) and (e)). Thus, we deduce that CO can reduce Rh³⁺ to Rh^{γ+}, and Mn⁴⁺ to Mn³⁺ with CO₂ production. On introducing additional H₂ and C₃H₆, Rh^{γ+} and Mn³⁺ can be further reduced to Rh^{δ+} and Mn²⁺, respectively. Figure S14 further suggested that oxygen vacancy and Ce³⁺ are also increased under reaction condition. Based on these, the mechanism for active species formation is proposed in Fig. 5(f), in which highly dispersed Rh-MnOx species are transformed to (CO)Rh^{δ+}-Mn²⁺(CO)x as pair active species under the reaction condition. The proposed active center structures are shown in Fig. 5(g). In contrast, on 2.5 % and 5 % Mn samples, MnOx nanoparticle is hard to be reduced to form Mn²⁺ (Figure S14~18).

We further investigated the reaction mechanism by performing an in-situ FTIR spectroscopy analysis. The catalyst was initially pretreated with CO and H₂, followed by purging with C₃H₆ while concurrently

recording the FTIR signal. The results (Fig. 6(a) and (c)) revealed that the band of Rh(CO) (2106 cm⁻¹), emerging from CO desorption from Rh(CO)₂, increased before decreasing, which is accompanied with the formation of butyraldehyde (1700 cm⁻¹), indicating Rh(CO) is the active species to attack C₃H₆ to form butyraldehyde. The rate of Rh(CO)₂ consumption to produce active Rh(CO) species is greater on Rh/1 % MnOx-CeO₂ than on Rh/CeO₂. This is evidenced by the persistence of peaks associated with Rh(CO)₂ (2070 and 1992 cm⁻¹) on Rh/CeO₂ even after an 8-minute reaction period, as shown in Fig. 6(b). On the contrary, these peaks (2077 and 2009 cm⁻¹) almost vanish after just 7 minutes of reaction on Rh/1 %MnOx-CeO₂, as depicted in Fig. 6(d). Moreover, the consumption rate of formed Rh(CO) active species is also faster on Rh/1 %MnOx-CeO₂ than on Rh/CeO₂. This is evidenced by the complete consumption of Rh(CO) on the former catalyst within 4 minutes, while the same species continues to exist on the latter catalyst even after an 8-minute reaction. In short, the formation and consumption of Rh(CO), in conjunction with butanal, happened in a higher rate on Rh/1 %MnOx-CeO₂ than on Rh/CeO₂. The improved hydroformylation activity of Rh/1 %MnOx-CeO₂ compared to Rh/CeO₂ is driven by an enhanced turnover rate of the key Rh(CO) active species. This enhancement is attributed to the adjacent MnOx weakening the CO adsorption strength on Rh^{δ+}, facilitating CO desorption from Rh(CO)₂ and subsequent formation of Rh(CO) active species. This process also aids the consumption of the formed Rh(CO) active species, where CO desorbs and reacts with activated propylene, leading to butanal formation.

The in-situ FTIR results for Rh/0.5 %MnOx-CeO₂ showed that the turnover of active Rh(CO) species is slower than that on Rh/1 %MnOx-CeO₂, for Rh/2.5 %MnOx-CeO₂ which showed no formation of Rh-MnOx species and much lower activity (Figure S19). We also record the FTIR spectra for catalysts after reaction under Ar purging and find the regeneration of Rh(CO)₂ species after reaction on Rh-MnOx catalysts (Figure S20 and S21). Based on these findings, we proposed the hydroformylation reaction mechanism on Rh-MnOx as shown in Scheme S2.

4. Conclusion

In conclusion, a combination of EXAFS, CO-FTIR, and HAADF-STEM characterizations confirm that on SEA method prepared Rh/y %MnOx-CeO₂ catalysts, Rh is atomically dispersed on the CeO₂ support with neighboring MnOx clusters when Mn loading is less than 1 %. These well-dispersed MnOx clusters are easily reduced to Mn²⁺ under reaction conditions, forming Rh-MnOx pair sites that enable the generation of electronically deficient Rh species. The resultant Rh^{δ+} (1 < δ < 2) cations, characterized by weakened CO adsorption strength, ease the desorption of CO from Rh, facilitating the activation of propane during the rate-determining step. Our *pseudo* in-situ XPS and in-situ FTIR findings suggest H₂, CO and C₃H₆ co-adsorption on Rh assist in reducing the Mn=O bond to create Rh-MnOx pair active sites, which only happen in the case of highly dispersed MnOx, not MnO₂ nanoparticles.

This study establishes Rh-MnOx pair active sites on the CeO₂ surface, demonstrating enhanced activity compared to the Rh single atom catalyst for propylene hydroformylation. The findings offer insights for the modification of single atom active sites using inorganic cluster as electronic ligands to improve hydroformylation activity.

CRediT authorship contribution statement

Ying Zheng: Conceptualization, Methodology, Validation, Formal analysis, Investigation, Data curation, Writing – original draft, Visualization. **Qi Yang:** Methodology, Formal analysis. **Sikai Wang:** Formal analysis. **Shinya Furukawad:** Resources, Formal analysis. **Maoshuai Li:** Conceptualization, Resources, Writing – review & editing, Supervision, Project administration, Funding acquisition. **Ning Yan:** Resources, Writing – review & editing, Supervision. **Xinbin Ma:** Conceptualization, Resources, Writing – review & editing, Supervision, Project

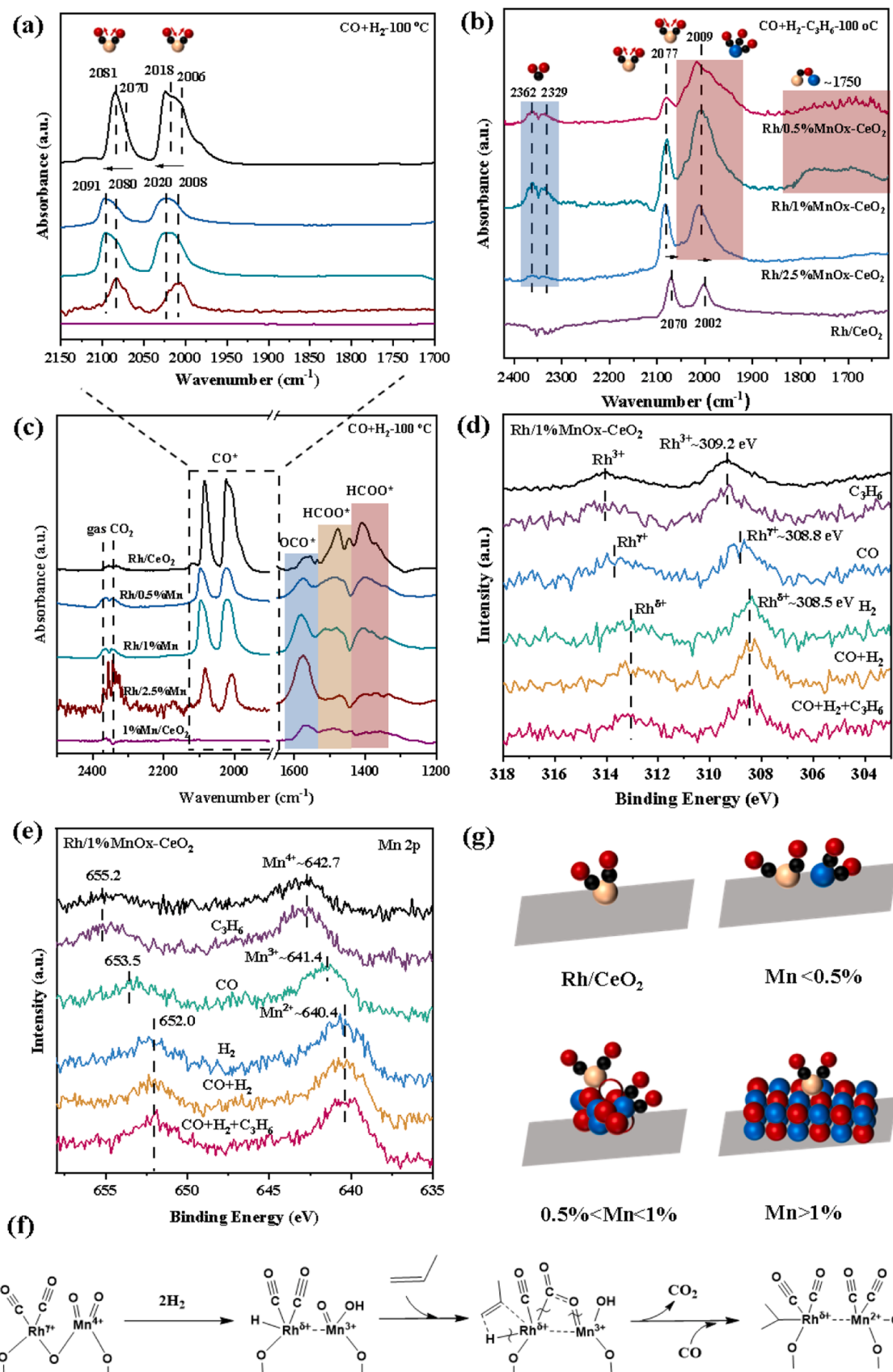


Fig. 5. (a) Magnified picture of (c) in range of 1700 – 2150 cm^{-1} . (c) FTIR spectra for different catalysts after treatment by CO and H_2 at 100°C . (b) The FTIR results of different $\text{Rh}/y\%$ MnO_x-CeO₂ catalysts after in-situ reaction co-feeding with CO , H_2 and C_3H_6 . (d) Rh 3d XPS results after different gas atmosphere treating for $\text{Rh}/1\%$ MnO_x-CeO₂ catalyst. (e) Mn 2p XPS spectra after different gas atmosphere treating for $\text{Rh}/1\%$ MnO_x-CeO₂ catalyst. (f) Proposed possible formation process of initial Rh-Mn dual metal active sites. (g) Proposed Rh-MnO_x active species structure on $\text{Rh}/y\%$ MnO_x-CeO₂ catalyst surface with different loading of Mn.

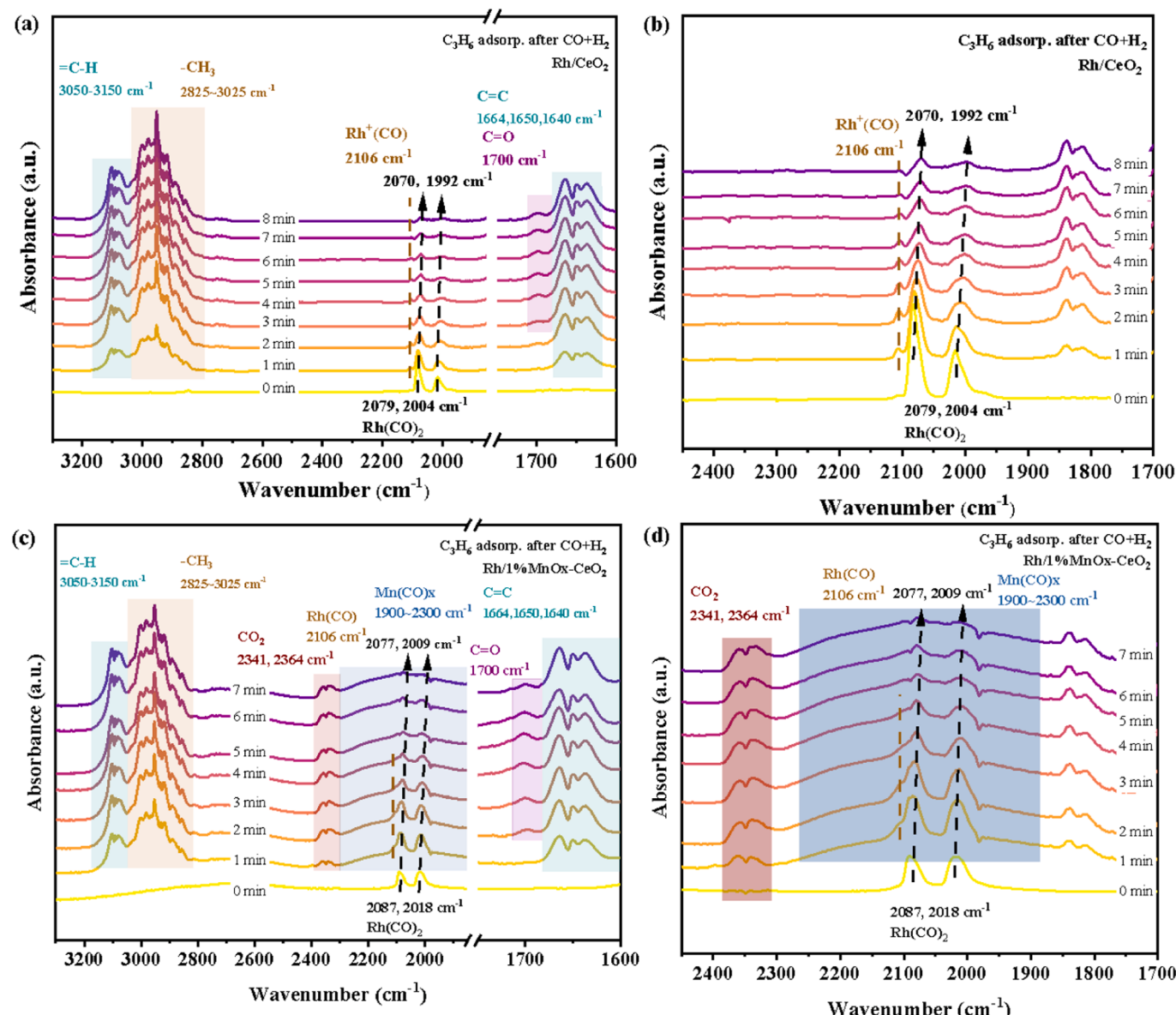


Fig. 6. *In-situ* FTIR spectra and the corresponding magnified spectra in the range of 2450 ~1700 cm⁻¹ (usually CO adsorbed species existed) for (a) and (b) Rh/CeO₂ and (c) and (d) Rh/1 %MnOx-CeO₂ which are firstly treated by CO and H₂ at 100 °C for 1 h, then purging with C₃H₆ and meanwhile recording the FTIR signal.

administration, Funding acquisition.

Declaration of Competing Interest

The authors declare that they have no known competing financial interests or personal relationships that could have appeared to influence the work reported in this paper.

Data availability

Data will be made available on request.

Acknowledgment

This work was supported by the National Key Research and Development Program of China (2018YFA0704501), Haihe Laboratory of Sustainable Chemical Transformations (CYZC202101), and the JSPS-NUS Collaboration Project supported by Japan and Singapore (A-0009191-00-00). We also thank the approval of JASRI (Proposal No.

2022B0528) to use beamline BL14B2 at SPring-8 (Japan Synchrotron Radiation Research Institute, Hyogo, Japan) for XAS measurement.

Appendix A. Supporting information

Supplementary data associated with this article can be found in the online version at doi:10.1016/j.apcatb.2024.123923.

References

- [1] S. Hanf, L. Alvarado Rupflin, R. Gläser, S.A. Schunk, Current state of the art of the solid Rh-based catalyzed hydroformylation of short-chain olefins, *Catalysts* 10 (2020) 1–36.
- [2] B. Liu, Y. Wang, N. Huang, X. Lan, Z. Xie, J.G. Chen, T. Wang, Heterogeneous hydroformylation of alkenes by Rh-based catalysts, *Chem* 8 (2022) 1–29.
- [3] R. Lang, T. Li, D. Matsumura, S. Miao, Y. Ren, Y. Cui, Y. Tan, B. Qiao, L. Li, A. Wang, X. Wang, T. Zhang, Hydroformylation of olefins by a Rhodium single-atom catalyst with activity comparable to RhCl(PPh₃)₃, *Angew. Chem. Int. Ed.* 55 (2016) 16054–16058.
- [4] L. Wang, W. Zhang, S. Wang, Z. Gao, Z. Luo, X. Wang, R. Zeng, A. Li, H. Li, M. Wang, X. Zheng, J. Zhu, W. Zhang, C. Ma, R. Si, J. Zeng, Atomic-level insights in

- optimizing reaction paths for hydroformylation reaction over Rh/CoO single-atom catalyst, *Nat. Commun.* 7 (2016) 14036.
- [5] J. Zhang, P. Sun, G. Gao, J. Wang, Z. Zhao, Y. Muhammad, F. Li, Enhancing regioselectivity via tuning the microenvironment in heterogeneous hydroformylation of olefins, *J. Catal.* 387 (2020) 196–206.
- [6] X.-F. Yang, A. Wang, B. Qiao, J. Li, J. Liu, T. Zhang, Single-atom catalysts: a new frontier in heterogeneous catalysis, *Acc. Chem. Res.* 46 (2013) 1740–1748.
- [7] H. Zhang, G. Liu, L. Shi, J. Ye, Single-atom catalysts: emerging multifunctional materials in heterogeneous catalysis, *Adv. Energy Mater.* 8 (2018) 1701343–1701367.
- [8] R.F. Heck, D.S. Breslow, Mechanism of the hydroformylation of olefins, *Chem. Ind. (Lond.)* 17 (1960).
- [9] R.F. Heck, D.S. Breslow, The reaction of cobalt hydrotetracarbonyl with olefins, *J. Am. Chem. Soc.* 83 (1961) 4023–4027.
- [10] B. Liu, N. Huang, Y. Wang, X. Lan, T. Wang, Insights into the activity screening and hydroformylation kinetics of Rh-based bimetallic phosphides, *ACS Catal.* (2021) 15235–15243.
- [11] J. Amsler, B.B. Sarma, G. Agostini, G. Prieto, P.N. Plessow, F. Studt, Prospects of heterogeneous hydroformylation with supported single atom catalysts, *J. Am. Chem. Soc.* 142 (2020) 5087–5096.
- [12] E. Zuiderma, L. Escorihuela, T. Eichelsheim, J.J. Carbo, C. Bo, P.C.J. Kamer, P.W.N. M. van Leeuwen, The rate-determining step in the Rhodium-xanthphos-catalysed hydroformylation of 1-octene, *Chem. Eur. J.* 14 (2008) 1843–1853.
- [13] S. Walter, H. Spohr, R. Franke, W. Hieringer, P. Wasserscheid, M. Haumann, Detailed investigation of the mechanism of Rh-diphosphite supported ionic liquid phase (silp)-catalyzed 1-butene hydroformylation in the gas phase via combined kinetic and density functional theory (DFT) modeling studies, *ACS Catal.* 7 (2017) 1035–1044.
- [14] H. Tricas, O. Diebolt, P.W.N.M. van Leeuwen, Bulky monophosphite ligands for ethene hydroformylation, *J. Catal.* 298 (2013) 198–205.
- [15] N. Huang, B. Liu, X. Lan, T. Wang, Insights into the bimetallic effects of a RhCo catalyst for ethene hydroformylation: Experimental and DFT investigations, *Ind. Eng. Chem. Res.* 59 (2020) 18771–18780.
- [16] I. Ro, M. Xu, G.W. Graham, X. Pan, P. Christopher, Synthesis of heteroatom Rh-ReO_x atomically dispersed species on Al₂O₃ and their tunable catalytic reactivity in ethylene hydroformylation, *ACS Catal.* 9 (2019) 10899–10912.
- [17] I. Ro, J. Qi, S. Lee, M. Xu, X. Yan, Z. Xie, G. Zakem, A. Morales, J.G. Chen, X. Pan, D.G. Vlachos, S. Caratzoulas, P. Christopher, Bifunctional hydroformylation on heterogeneous Rh-WO_x pair site catalysts, *Nature* 609 (2022) 287–292.
- [18] Y. Zheng, Q. Wang, Q. Yang, S. Wang, M.J. Hulse, S. Ding, S. Furukawa, M. Li, N. Yan, X. Ma, Boosting the hydroformylation activity of a Rh/CeO₂ single-atom catalyst by tuning surface deficiencies, *ACS Catal.* 13 (2023) 7243–7255.
- [19] L. Alvarado Rupflin, J. Mormul, M. Lejkowski, S. Titlbach, R. Papp, R. Gläser, M. Dimitrakopoulou, X. Huang, A. Trunschke, M.G. Willinger, R. Schlögl, F. Rosowski, S.A. Schunk, Platinum group metal phosphides as heterogeneous catalysts for the gas-phase hydroformylation of small olefins, *ACS Catal.* 7 (2017) 3584–3590.
- [20] R.M. Deshpande, A.A. Kelkar, A. Sharma, C. Julcour-Lebigue, H. Delmas, Kinetics of hydroformylation of 1-octene in ionic liquid-organic biphasic media using rhodium sulfoxantphos catalyst, *Chem. Eng. Sci.* 66 (2011) 1631–1639.
- [21] D.G. Hanna, S. Shylesh, S. Werner, A.T. Bell, The kinetics of gas-phase propene hydroformylation over a supported ionic liquid-phase (silp) rhodium catalyst, *J. Catal.* 292 (2012) 166–172.
- [22] Z. Mao, Z. Xie, J.G. Chen, Comparison of heterogeneous hydroformylation of ethylene and propylene over RhCo₃/MCM-41 catalysts, *ACS Catal.* 11 (2021) 14575–14585.
- [23] B. Liu, N. Huang, Y. Wang, X. Lan, T. Wang, Promotion of inorganic phosphorus on Rh catalysts in styrene hydroformylation: Geometric and electronic effects, *ACS Catal.* 11 (2021) 1787–1796.
- [24] S. Lee, A. Patra, P. Christopher, D.G. Vlachos, S. Caratzoulas, Theoretical study of ethylene hydroformylation on atomically dispersed Rh/Al₂O₃ catalysts: reaction mechanism and influence of the ReO_x promoter, *ACS Catal.* 11 (2021) 9506–9518.
- [25] M.G. Farpon, W. Henao, P.N. Plessow, E. Andres, R. Arenal, C. Marini, G. Agostini, F. Studt, G. Prieto, Rhodium single-atom catalyst design through oxide support modulation for a selective gas-phase ethylene hydroformylation, *Angew. Chem. Int. Ed.* 62 (2022) e202214048.
- [26] T. Li, F. Chen, R. Lang, H. Wang, Y. Su, B. Qiao, A. Wang, T. Zhang, Styrene hydroformylation with in situ hydrogen: Regioselectivity control by coupling with the low-temperature water–gas shift reaction, *Angew. Chem. Int. Ed.* 59 (2020) 7430–7434.
- [27] M. Chen, G. Gupta, C.W. Ordóñez, A.R. Lamkins, C.J. Ward, C.A. Abolafia, B. Zhang, L.T. Roling, W. Huang, Intermetallic nanocatalyst for highly active heterogeneous hydroformylation, *J. Am. Chem. Soc.* 143 (2021) 20907–20915.
- [28] W. Mao, J. Su, Z. Zhang, X. Xu, W. Dai, D. Fu, J. Xu, X. Zhou, Y. Han, Kinetics study of C²⁺ oxygenates synthesis from syngas over Rh–MnO_x/SiO₂ catalysts, *Chem. Eng. Sci.* 135 (2015) 312–322.
- [29] P. Preikschas, J. Bauer, X. Huang, S. Yao, R. Naumann-Alnoncourt, R. Krahnert, A. Trunschke, F. Rosowski, M. Driess, From a molecular single-source precursor to a selective high-performance RhMnO_x catalyst for the conversion of syngas to ethanol, *ChemCatChem* 11 (2019) 885–892.
- [30] M. Ojeda, M.L. Granados, S. Rojas, P. Terreros, F.J. García-García, J.L.G. Fierro, Manganese-promoted Rh/Al₂O₃ for C₂-oxygenates synthesis from syngas: effect of manganese loading, *Appl. Catal. A-Gen.* 261 (2004) 47–55.
- [31] F.G.A. van den Berg, J.H.E. Glezer, W.M.H. Sachtle, The role of promoters in CO H₂ reactions: effects of MnO and MoO₂ in silica-supported rhodium catalysts, *J. Catal.* 93 (1985) 340–352.
- [32] Q. Sun, B.W.J. Chen, N. Wang, Q. He, A. Chang, C.M. Yang, H. Asakura, T. Tanaka, M.J. Hulsey, C.H. Wang, J. Yu, N. Yan, Zeolite-encaged Pd-Mn nanocatalysts for CO (2) hydrogenation and formic acid dehydrogenation, *Angew. Chem. Int. Ed. Engl.* 59 (2020) 20183–20191.
- [33] K. Yu, L.L. Lou, S. Liu, W. Zhou, Asymmetric oxygen vacancies: the intrinsic redox active sites in metal oxide catalysts, *Adv. Sci.* 7 (2020) 1901970.
- [34] X. Lin, S. Li, H. He, Z. Wu, J. Wu, L. Chen, D. Ye, M. Fu, Evolution of oxygen vacancies in MnO_x-CeO₂ mixed oxides for soot oxidation, *Appl. Catal. B: Environ.* 223 (2018) 91–102.
- [35] J. Liu, Y. Zheng, Q. Zhu, Y. Dong, S. Lu, B. Peng, Y. Chen, S. Zeng, K. Li, MnO_x-CeO₂ derived from Mn-Ce-MOFs with highly efficient removal of formaldehyde, *Catal. Surv. Asia* 24 (2020) 207–218.
- [36] J.R. Regalbuto, Electrostatic adsorption, *Synth. Solid Catal.* (2009) 33–58.
- [37] L. Jiao, J.R. Regalbuto, The synthesis of highly dispersed noble and base metals on silica via strong electrostatic adsorption: I. Amorphous silica, *J. Catal.* 260 (2008) 329–341.
- [38] L.F. Nascimento, O.A. Serra, Washcoating of cordierite honeycomb with Ceria-Copper mixed oxides for catalytic diesel soot combustion, *Process Saf. Environ. Prot.* 101 (2016) 134–143.
- [39] O.H. Laguna, M.A. Centeno, F. Romero-Sarria, J.A. Odriozola, Oxidation of CO over gold supported on Zn-modified Ceria catalysts, *Catal. Today* 172 (2011) 118–123.
- [40] Z.-Y. Pu, J.-Q. Lu, M.-F. Luo, Y.-L. Xie, Study of oxygen vacancies in Ce_{0.9}Pr_{0.1}O_{2-δ} solid solution by in situ x-ray diffraction and in situ raman spectroscopy, *J. Phys. Chem. C* 111 (2007) 18695–18702.
- [41] P. Zhang, H. Lu, Y. Zhou, L. Zhang, Z. Wu, S. Yang, H. Shi, Q. Zhu, Y. Chen, S. Dai, Mesoporous MnCeO_x solid solutions for low temperature and selective oxidation of hydrocarbons, *Nat. Commun.* 6 (2015) 8446.
- [42] P. Chatterjee, D. Mukherjee, A. Sarkar, A.K. Chakraborty, Mn-doped CeO₂-CNT nanohybrid for removal of water soluble organic dyes, *Appl. Nanosci.* 12 (2022) 3031–3043.
- [43] Z. Luo, Z. Zhu, Effects of support preparation methods on structural and catalytic properties of Au/MnO_x-CeO₂, *Catal. Lett.* 154 (2024) 422–429.
- [44] W. Hu, F. He, X. Chen, S. Liu, Hydrothermal synthesis of leaf-like CeO₂ nanosheets and its MnO_x/CeO₂ composites for catalytic combustion of chlorobenzene, *J. Nanopart. Res.* 21 (2019) 1–14.
- [45] H. Huang, J. Liu, P. Sun, S. Ye, B. Liu, Effects of mn-doped ceria oxygen-storage material on oxidation activity of diesel soot, *RSC Adv.* 7 (2017) 7406–7412.
- [46] Y.-F. Qu, J.-X. Guo, Y.-H. Chu, M.-C. Sun, H.-Q. Yin, The influence of mn species on the SO₂ removal of Mn-based activated carbon catalysts, *Appl. Surf. Sci.* 282 (2013) 425–431.
- [47] S. Bai, F. Liu, B. Huang, F. Li, H. Lin, T. Wu, M. Sun, J. Wu, Q. Shao, Y. Xu, X. Huang, High-efficiency direct methane conversion to oxygenates on a cerium dioxide nanowires supported rhodium single-atom catalyst, *Nat. Commun.* 11 (2020) 954.
- [48] D. Wu, S. Liu, M. Zhong, J. Zhao, C. Du, Y. Yang, Y. Sun, J. Lin, S. Wan, S. Wang, J. Huang, Y. Yao, Z. Li, H. Xiong, Nature and dynamic evolution of rh single atoms trapped by CeO₂ in CO hydrogenation, *ACS Catal.* 12 (2022) 12253–12267.
- [49] J. Xu, Y. Wang, K. Wang, M. Zhao, R. Zhang, W. Cui, L. Liu, M.S. Bootharaju, J. H. Kim, T. Hyeon, H. Zhang, Y. Wang, S. Song, X. Wang, Single-atom Rh on high-index CeO₂ facet for highly enhanced catalytic CO oxidation, *Angew. Chem. Int. Ed.* 62 (2023) e202302877.
- [50] H. Zhu, Y. Li, X. Zheng, In-situ drifts study of CeO₂ supported rh catalysts for N₂O decomposition, *Appl. Catal. A: Gen.* 571 (2019) 89–95.
- [51] T. Huang, M. Shen, G. Cheng, Y. Wang, J. Wang, W. Li, S.H. Oh, G. Qi, M. Yang, J. Wang, Possible negative influences of increasing content of Cerium on activity and hydrothermal stability of Rh/Ceria-Zirconia three-way catalysts, *J. Rare Earths* 39 (2021) 797–804.
- [52] L. Lutsenko, L. Oleksenko, G. Telbiz, V. Gerasova, Catalytic activity in CO oxidation of MnO_x supported on oxide and zeolite carriers, *Fr. -Ukr. J. Chem.* 3 (2015) 54–64.
- [53] M. Feng, Fan Yang, Jianping Wang, Vibrational and structural dynamics of Mn (CO)₅Br and Re(CO)₅Br examined using nonlinear infrared spectroscopy, *Chin. J. Chem. Phys.* 29 (2016) 81–86.
- [54] A.S. Lisitsyn, S.A. Stevenson, H. Knözinger, Carbon monoxide hydrogenation on supported Rh-Mn catalysts, *J. Mol. Catal.* 63 (1990) 201–211.
- [55] S.A. Stevenson, A. Lisitsyn, H. Knözinger, Adsorption of carbon monoxide on Manganese-promoted Rhodium/Silica catalysts as studied by infrared spectroscopy, *J. Phys. Chem.* 94 (1990) 1576–1581.
- [56] X. Sun, H. Jansma, T. Miyama, R.D. Sanjeeva Aluthege, K. Shinmei, N. Yagihashi, H. Nishiyama, D. Osadchii, B. van der Linden, M. Makkee, Unveiling the structure sensitivity for direct conversion of syngas to C₂-oxygenates with a multicomponent-promoted Rh catalyst, *Catal. Lett.* 150 (2020) 482–492.
- [57] A.S. Lisitsyn, S.A. Stevenson, H. Knözinger, Carbon monoxide hydrogenation on supported Rh-Mn catalysts, *J. Mol. Catal.* 63 (1990) 201–211.